

Sensing methodology for *in vivo* stability evaluation of total hip and knee arthroplasty

Shiyong Hao^{a,*}, John T. Taylor^a, Chris R. Bowen^b, Sabina Gheduzzi^b, Anthony W. Miles^b

^a Department of Electronic and Electrical Engineering, University of Bath, BA2 7AY, UK

^b Department of Mechanical Engineering, University of Bath, BA2 7AY, UK

ARTICLE INFO

Article history:

Received 20 July 2009

Received in revised form 9 October 2009

Accepted 14 October 2009

Available online 23 October 2009

Keywords:

THA

Implantable

In vivo

Micromotion

Migration

Calibration

ABSTRACT

This paper describes an implantable, remotely interrogated system for the *in vivo* measurement of both micromotion and migration in applications such as *total hip arthroplasty* (THA) and *total knee arthroplasty* (TKA). These metrics are the primary indicators of post-operative implant stability and their easy availability represents an important advance in the ability of clinicians to assess the long-term stability of the implants and also to plan and optimise patients' rehabilitation protocols. The system is based on a modified form of *differential variable reluctance transducer* (DVRT) whose null-point is set automatically by means of a self-calibration algorithm. The self-calibration process not only allows the measuring bridge to work at maximum accuracy (i.e. for micromotion measurements) but also automatically records gross changes in position (migration). Simulations and preliminary measurements show that the calibration algorithm works correctly in spite of component tolerances and initial set up errors, and that the device can measure micromotion with an amplitude as low as 1 μm with a gross displacement (migration) in the range 0 to $\pm 4\text{mm}$.

© 2009 Elsevier B.V. All rights reserved.

1. Introduction

Modern THA, *total hip arthroplasty* or *total hip replacement*, was first performed by John Charnley in the 1960s [1]. It is now seen as one of the most important surgical advances of the 20th century, with 50,000 hips replaced in the UK with an overall cost of £140 million per annum [2]. Furthermore, TKA, *total knee arthroplasty*, which has been developed over last thirty years, is challenging THA in terms of volume. It is reported by the UK National Health Service (NHS) that more than 70,000 knee replacements were carried out in England and Wales in 2007 [3]. These numbers will increase in future as THA and TKA become more and more accepted, due to their contributions to both pain relief and function improvement in patients. The outcomes of such surgery are also encouraging: the satisfaction rate as reported in previous investigations [4,5] is more than 80% after primary TKA, and Ng [6] and Ramiah [7] claimed that quality of patients' lives has been improved and sustained up to five years after THA. Many other studies have also verified that THA and TKA are highly beneficial and cost-effective procedures [8,9].

In spite of this success, a high post-operative failure rate has been increasingly reported in recent years. Failure rates ranging from 10 to 20% for knee prostheses during the first five years have

been shown Ranawat [10] and Skolnick [11]. Similarly, Losina [12] found that 4.4% of prostheses failed by the end of the fifth year after primary THA. These failed implants usually led to *revision surgery*, which in addition to being more expensive than the initial procedures has inevitable adverse effects such as higher operative complication rate and a reduction in prosthesis durability [13]. As a result, much effort has been made during last few decades to understand better the failure mechanisms involved. This has led to corresponding technical advances which have improved prosthesis design for long-term survival.

Many investigators consider aseptic loosening, either symptomatic or asymptomatic, to be the most common failure mode in both THA [14,17] and TKA [15,16]. Nixon [13] reported that aseptic loosening is the cause of 70% of THA revision procedures; in Ducheyne's survey [16] loosened knee implants accounted for 5.8%. There are many technical and biological factors that contribute to the loosening [16], in which particulate wear debris is the major one in THA [17], while mal-alignment is prevalent in TKA [15]. Since aseptic loosening is one of the most common failure modes, the extent of post-operative implant stability, which largely determines the incidence of loosening, is an important predictor of durability for both cemented and, in particular, uncemented prostheses which rely on bone ingrowth for long-term fixation [18,19,21]. In addition, it is also important to reduce the risk of long-term failure of implants [20].

Prostheses with inadequate stability tend to suffer from excessive motion at the prosthesis-bone or cement-bone interface under

* Corresponding author. Tel.: +44 1225386071.
E-mail address: sh258@bath.ac.uk (S. Hao).

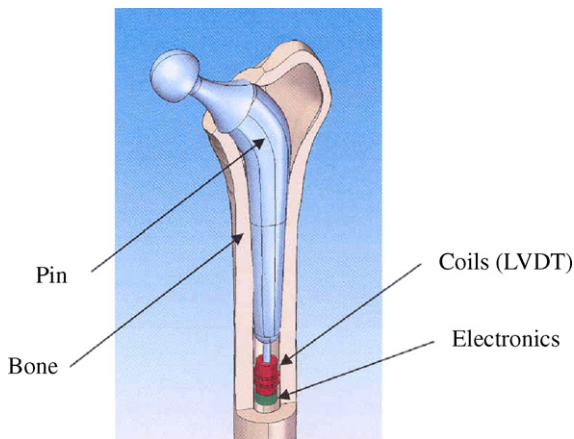


Fig. 1. Placement of the device in total hip arthroplasty (THA).

daily weight-bearing loads [21], leading to ultimate failure. As a result the post-operative stability of implants is quantified in terms of their post-operative *migration* and *micromotion*. *Migration* is the nonrecoverable movement of the implant slowly embedding itself into the host tissue as a consequence of loading. *Micromotion*, on the other hand, is the recoverable relative movement between implant and bone associated with the elasticity of the construct. Evidence suggests that early implant micromotion of uncemented hip implants is strongly correlated with clinical loosening and hence premature failure [22]. This is because excessive movement will inhibit bone ingrowth into the porous surface, which is the base of the biological fixation [21].

There have been many studies that focus on the post-operative stability prediction of implants by measuring their migration. Imaging techniques such as *Roentgen stereophotogrammetric analysis* (RSA) were generally used in early investigations [11,23], however their applications are constrained by poor resolution ($>100\ \mu\text{m}$). More recently *in vitro* methods of measurement have been developed to evaluate implants in cadaveric or synthetic bone models to evaluate implant migration and micromotion [24,25]. These systems employ a *linear variable differential transformer* (LVDT) device together with loading configurations using artificial bone. In such tests a precision of $5\ \mu\text{m}$ can be reached [26].

In spite of the availability of methods for monitoring migration, there is currently no method for direct *in vivo* measurement of implant *micromotion*. In this paper we describe a device which provides the first combined *in vivo* measurement of both micromotion and migration in the context of applications such as THA and TKA. The system, which is based on a modified DVRT (*differential variable reluctance transducer*), is mounted in the bone cavity as indicated in Fig. 1 (for THA) and has no direct contact with the implant. Control, data transmission and power supply will be provided by means of a telemetry system, although these aspects are not discussed.

Whilst it is well known that bridge-based position sensors are very sensitive when exactly balanced, it is difficult to install such devices in an application such as we describe given the unavoidable component tolerances and the imperfections of surgical assembly. In order to overcome these critical problems, we describe an electronic self-calibration method which allows the bridge to function at maximum precision even in the presence of significant component tolerances. Apart from allowing precise measurements of micromotion to be made, the action of the self-calibration algorithm requires a record to be kept of gross changes in the position of the balance point of the bridge. This record provides a convenient and accessible measure of *migration* [27]. Taken together, the methods proposed to measure micromotion and migration are

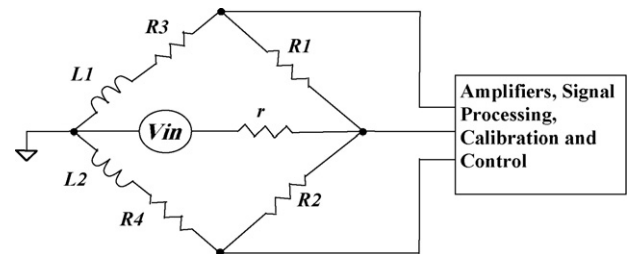


Fig. 2. Circuit schematic showing the form of the DVRT and its connection to the signal processing electronics (the series resistance of the coils r_L are not shown in the figure).

somewhat analogous to *small-* and *large-signal* analysis in conventional analogue circuit theory.

This paper presents an in-depth analysis of the operation of the system validated by detailed bench measurements. These measurements indicate a limiting axial resolution of about $1\ \mu\text{m}$ for micromotion with the additional advantage of providing a record of long-term implant settling (migration) in the range $-4\ \text{mm}$ to $+4\ \text{mm}$. Although the system as described in this paper is designed for measuring the motion of the stem in the axial direction at the prosthesis–bone interface, it can in principle be adapted to detect motion in other planes.

The paper is organised as follows. Section 2 provides an overview of the theory of the device while Section 3 focuses on the operation of the calibration algorithm. Section 4 describes the results of bench tests on the device and Section 5 discusses the limitations of the method and the assumptions that have been made in developing the theoretical treatment. Section 5 also considers in outline the requirements of an integrated version of the device suitable for implantation.

2. System configuration

2.1. Properties of the RL bridge

The system is based on a modified form of *differential variable reluctance transducer* (DVRT). Fig. 2 is the circuit schematic of the DVRT showing its connection to the signal processing electronics and Fig. 3 shows typical dimensions for use in THA. The circuit consists of a pair of coaxial cylindrical inductive coils L_1 and L_2 and two pairs of variable resistors R_1 , R_2 and R_3 , R_4 connected to form an *RL*-Wheatstone bridge. A short ferrite rod attached to the implant engages with the coils along their axis, while the coils themselves are attached to the bone. The bridge is driven by a voltage controlled sinusoidal oscillator (VCO) of amplitude V_{in} , internal resistance r and frequency, f . V_{in} was chosen to be about $100\ \text{mV}$ and f about $100\ \text{kHz}$ since these values can be conveniently generated by a CMOS VCO in integrated circuit form. In addition, this

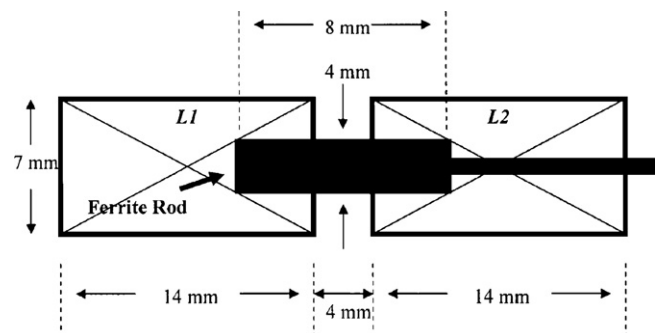


Fig. 3. Approximate coil and ferrite rod dimensions for use in THA.

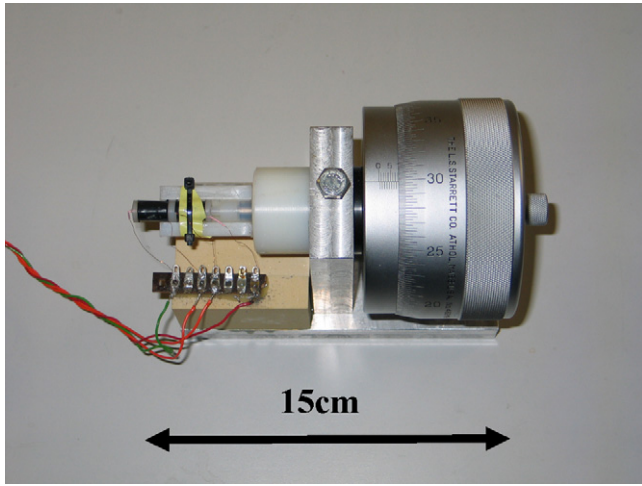


Fig. 4. Arrangement for bench-testing. The co-axial bridge coils (scaled for total hip arthroplasty (THA); cf Figs. 1–3) are on the left of the picture and the ferrite rod is connected to the micrometer gauge on the right. The limiting resolution of this micrometer is 1 μm .

choice of operating frequency requires resistors of a few hundred ohms (which can be easily realised in integrated circuit form as either fixed or variable components) and inductors of about 1 mH which can be realised as cylindrical coils sufficiently small for implantation (operation at lower frequencies is also considered). The outputs of the bridge and the VCO are both required as inputs to the signal processing circuitry.

The experimental results reported in this paper were obtained from a bench model with the dimensions of Fig. 3. A photograph of the bench model is shown in Fig. 4. L_1 and L_2 each consisted of a 5-layer coil of 38 SWG insulated copper wire (about 400 turns in total) with a coupling coefficient k and series resistance, r_L . The ferrite rod is a standard cylindrical component with a relative permeability (μ) of 48, resulting in a self-inductance of about 800 μH , a typical mutual inductance of about 165 μH and a series resistance of about 11 Ω .

The signal processing employed in the bench experiments was very simple consisting a signal generator (for the VCO), an amplifier for the bridge output, gain about 500 and bandwidth about 200 kHz, the outputs being read on an oscilloscope. The variable resistors were multi-turn components which were adjusted manually according to the algorithm described below.

The transfer function of the bridge, $H_1(j\omega)$, is given by the following expression where ω is the angular frequency ($=2\pi f$; see Appendix A for the detailed derivation):

$$H_1(j\omega) = \frac{V_{o\text{-bridge}}(j\omega)}{V_{in}(j\omega)} = REAL + j.IMAG \quad (1)$$

where $V_{o\text{-bridge}}(j\omega)$ is the output voltage of the bridge (see Fig. 2) and $REAL$ and $IMAG$ are functions of R_{1-4} , $L_{1,2}$, k and ω . If A_v is the voltage gain of the amplifier, the overall transfer function of the system is:

$$H(j\omega) = A_v \cdot H_1(j\omega) = A_v(REAL + j.IMAG) \quad (2)$$

Initially the system is set so that $R_1 = R_2$ and $R_3 = R_4$. If the rod is then placed at the geometrical centre of the coils so that $L_1 = L_2$ the bridge is balanced and the output voltage is zero since both the terms $REAL$ and $IMAG$ in Eq. (1) are zero. However, in practice it is impossible to achieve this level of balance due to mis-positioning of the ferrite rod as a result of imprecision in the surgical assembly and/or tolerances in the values of the inductors and other components. In consequence, it is impossible to determine either the static displacement (misalignment) of the core once the system has

been implanted or its gross movement thereafter (migration), thus reducing the effectiveness of the DVRT in this application. However, these problems are solved by means of the *calibration* procedure described in the next section.

3. Calibration and output analysis of the system

3.1. Calibration method

As already noted, the key problem is orientating the ferrite rod precisely at the geometrical centre of the coils so that at rest the inductors L_1 and L_2 are equal and the bridge is balanced giving zero output. If, as is generally the case, such mechanical precision is not feasible, we show that it is possible to bring the output of the bridge close to zero by adjusting the electrical parameters of the system, specifically the frequency f and the values of the four resistors R_1 , R_2 , R_3 , and R_4 . In practice, two of the resistors (say R_2 , R_4) can be preset to fixed values which simplifies the calibration process (the algorithm described below assumes this simplification. Suitable choices for these resistor values are discussed in Appendix C). Application of the method will also absorb tolerances in the component values generally. Note that if four variable resistors are employed, greater precision is possible at the expense of a more complex algorithm and an increased number of iterations.

One complication of the calibration process is that the real part and imaginary part of the transfer function $H_1(j\omega)$ of the bridge both depend on R_1 and R_3 (Eq. (1)), which means any variations in the real part or the imaginary part, caused by R_1 or R_3 , leads to changes in the other. Therefore, the adjustment of the real and imaginary parts must be repeated iteratively before the bridge is completely balanced, which raises the issue of *convergence* (see Appendix B). In practice, as described below, this is not a serious problem as the process converges to the required level of residual error after very few iterations.

To null the output to zero, with reference to Eq. (1) and the definition of terms given in Appendix A, we adopt the following procedure:

1. Sweep the oscillator frequency until the phase angle of $H_1(j\omega)$ is zero or 180° . This is the resonant frequency of the system and sets term $IMAG$ in (1) to zero.
2. Adjust R_1 until the phase angle of $H_1(j\omega)$ is 90° or -90° . This sets the term $REAL$ to zero.
3. Adjust R_3 until the phase angle of $H_1(j\omega)$ is zero or 180° . This sets term $IMAG$ to zero.
4. Repeat steps 2 and 3 until the output is zero.

The calibration process is terminated when $|H_1(j\omega)| < 2 \times 10^{-5}$.

In some cases, the calibration fails because the equations $REAL=0$ or $IMAG=0$ have no real solutions for R_1 , R_3 . Conditions for successful calibration are discussed in Section 5.

3.2. Output analysis of system

After calibration, the new values of R_1 , R_3 are R'_1 , R'_3 respectively, and hence the new values of $REAL$ and $IMAG$ defined in Eq. (1) are $REAL'$ and $IMAG'$. A key assumption in the theory which follows is that variations of L_1 , L_2 and M caused by small axial displacements, z , of the rod can be represented by the following set of linear equations:

$$\begin{aligned} L'_1 &= L_1 + m_1 z \\ L'_2 &= L_2 - m_2 z \\ M' &= M - m_3 z \end{aligned} \quad (3)$$

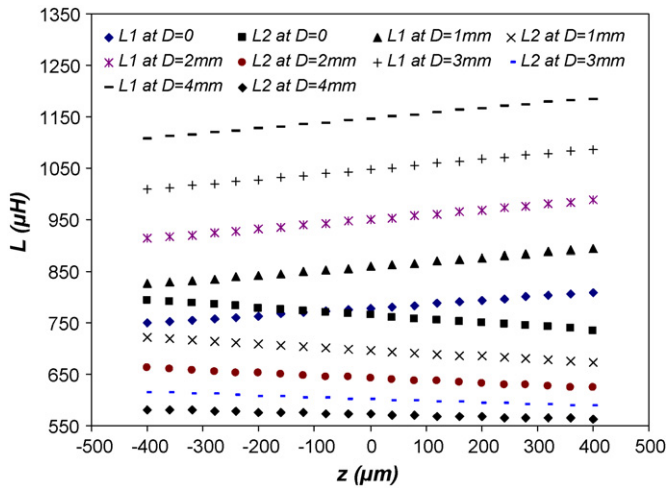


Fig. 5. Coil self-inductance. Measured values of L_1 , L_2 as a function of small axial displacements (micromotion) for five different values of initial position D (0, 1, 2, 3, 4 mm).

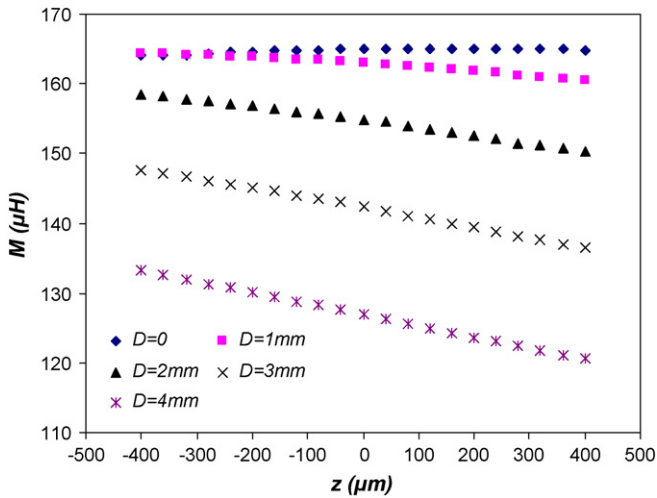


Fig. 6. Mutual inductance between L_1 , L_2 as a function of small axial displacements (micromotion) for five different values of the rod initial position D (0, 1, 2, 3, 4 mm).

where m_1 , m_2 and m_3 are constants. Substituting Eq. (3) into Eq. (2) and differentiating with respect to z :

$$\frac{\partial V_o}{\partial z} = A_v V_{in} \left(\frac{\partial REAL'}{\partial z} + j \frac{\partial IMAG'}{\partial z} \right) \quad (4)$$

where $\partial REAL'/\partial z$ and $\partial IMAG'/\partial z$ are functions of $R'_{1,3}$, $R_{2,4}$, $L_{1,2}$, k , $m_{1,2,3}$ and ω , which are constants after calibration is complete. Eq. (4) can also be written in polar form:

$$\frac{\partial V_o}{\partial z} = A_v V_{in} \left\{ \sqrt{\left(\frac{\partial REAL'}{\partial z} \right)^2 + \left(\frac{\partial IMAG'}{\partial z} \right)^2} \right\} \cdot e^{j\theta} \quad (5)$$

where $\theta = \arg(\partial V_o/\partial z)$.

From Eq. (5), it is apparent that V_o , the output voltage of the system, is proportional to the rod displacement z if Eq. (3) is valid, i.e., if a small-signal analysis can be applied (the validity of this key assumption has been tested experimentally and is discussed in Section 4.1). This allows the *micromotion* of the rod to be predicted from changes in the observed output voltage V_o and the output gradient (see Eqs. (4) and (5)).

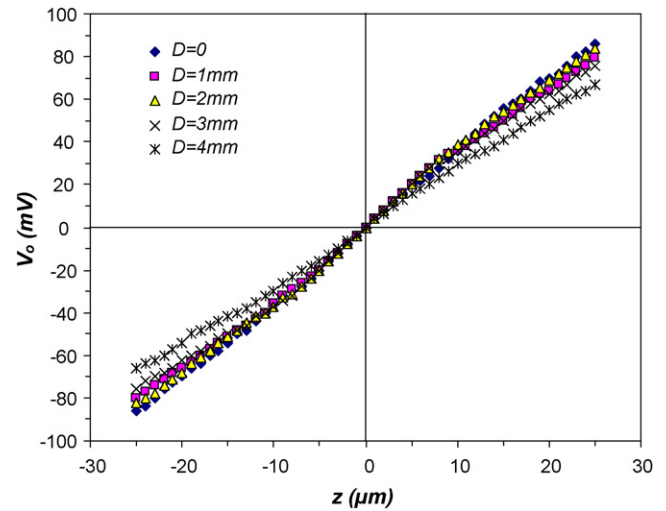


Fig. 7. Measured system output V_o as a function of small axial displacements (micromotion) (–25 to 25 μm) for different values of the initial offset D . All the cases show the response after calibration. $V_{in} = 0.1 \text{ V}$, $f = 100 \text{ kHz}$.

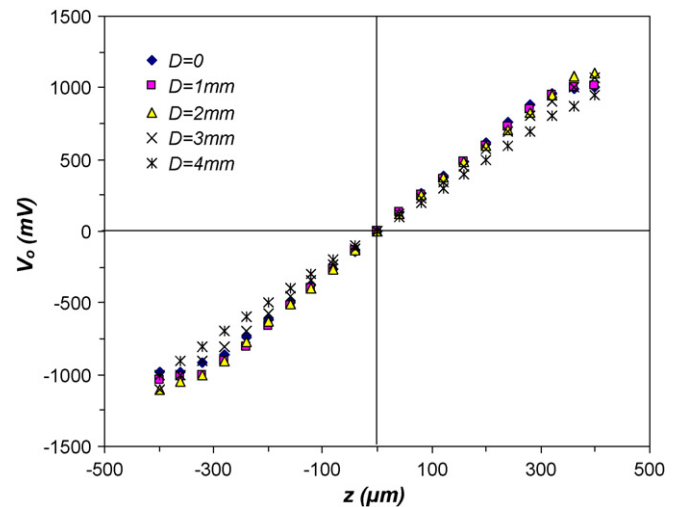


Fig. 8. Measured system output V_o as a function of small axial displacements (micromotion) (–400 to 400 μm) for different values of the initial offset D (migration). All the cases show the response after calibration. $V_{in} = 0.1 \text{ V}$, $f = 100 \text{ kHz}$.

Finally, once the calibration process is complete and the modified values of the resistors R'_1 , R'_3 are known, the gross axial displacement (migration) of the implant since the last calibration phase can be calculated. A 1-to-1 mapping relationship between the values of R'_1 , R'_3 and implant migration exists and hence the migration can be conveniently found using a look-up table. Furthermore, since a similar mapping process allows the values of L'_1 and L'_2 to be found, the polynomial functions $REAL'$ and $IMAG'$ can be determined and Eq. (5) can be solved. This provides the slope of the characteristic at the new operating (null) point and allows small changes in the output voltage due to *micromotion* to be translated into a measure of axial displacement.

It is important to note that the two modes of measurement are independent and so do not interfere with one another. This is because *migration* measurement is a consequence of the convergence of the calibration algorithm whereas *micromotion* is only measured once the system parameters have settled down. This point is expanded in Section 5.1 where the analogy to large- and small-signal circuit analysis is made. Note the ability to separate

migration and micromotion relies on the basic assumption that migration is a slow process compared to micromotion.

4. System implementation and results

A high precision micrometer head, with an accuracy of 1 μm, was used in our tests for micromotion adjustments and measurements. The micrometer head is combined with the pair of coils forming the bridge by means of a nylon holder mounted on a steel base. The ferrite rod is connected to the micrometer gauge to monitor its displacement. The coil pair is connected to four manually adjustable potentiometers to form a DVRT bridge, which is then connected to an amplifier system. A photograph of this system is shown in Fig. 4. The four potentiometers are multi-turn units variable between 0 and 1 kΩ.

The total gain of the amplifier is about 500 with a bandwidth of 200 kHz. A sine wave signal with 0.1 V amplitude and frequency of 100 kHz is applied to the input of the system and the output is monitored using an oscilloscope. The coil inductance and potentiometer values were measured using a high precision LCR meter with an accuracy of about 0.05%.

4.1. Coil self-inductance and mutual inductance

Figs. 5 and 6 show the measured variation of self-inductance and mutual inductance of the coils for small displacements of the rod (corresponding to micromotion). It is clear that a linear relationship between inductance L_1 , L_2 , M and displacement is preserved over a range of -400 to 400 μm even with initial gross displacements of the rod (migration; 0 to +4 mm in Figs. 5 and 6). This validates the key assumption expressed by Eq. (3), allowing a linearised *small-signal* model to be employed to predict micromotion in a range of about ±400 μm. Starting with the data in Figs. 5 and 6, curve fitting is used to determine the parameters of Eq. (3) (inductance values in μH) as a function of gross displacement, D :

$$\left. \begin{aligned} \left. \begin{aligned} L'_1 &= 779.04 + 0.0745z \\ L'_2 &= 764.56 - 0.0734z \\ M &= \begin{cases} 165.08 + 0.0025z & z \leq 0 \\ 165.05 - 0.0003z & z > 0 \end{cases} \end{aligned} \right\} @D = 0 \\ \left. \begin{aligned} L'_1 &= 859.68 + 0.0863z \\ L'_2 &= 697.07 - 0.0613z \\ M &= 162.74 - 0.005z \end{aligned} \right\} @D = 1 \text{ mm} \\ \left. \begin{aligned} L'_1 &= 950.16 + 0.0944z \\ L'_2 &= 642.24 - 0.048z \\ M &= 154.64 - 0.0104z \end{aligned} \right\} @D = 2 \text{ mm} \\ \left. \begin{aligned} L'_1 &= 1047.4 + 0.0989z \\ L'_2 &= 600.74 - 0.0348z \\ M &= 142.18 - 0.0142z \end{aligned} \right\} @D = 3 \text{ mm} \\ \left. \begin{aligned} L'_1 &= 1145.9 + 0.0976z \\ L'_2 &= 572.09 - 0.0229z \\ M &= 126.93 - 0.016z \end{aligned} \right\} @D = 4 \text{ mm} \end{aligned} \right\} (6)$$

Note: M can be considered as a constant when $D=0$.

4.2. Output voltage and small axial displacements (micromotion)

Once the self-calibration process is completed, the output voltage can be measured with the rod displacement adjusted by the micrometer head with an increment of 1 μm. The effect of implementing this procedure is shown in Figs. 7 and 8. Fig. 7 shows that the output is zero at $z=0$ and that the linearity is preserved over a range of values which is adequate for micromotion measurement. Note that the gradient varies slightly with D due to the changes in resistor values and coil inductance inherent in the process.

Table 1

A comparison of the calculated and measured gradients of the system output for different values of the initial offset D . Errors between them are also shown in the table.

D (mm)	0	2	3	4
Calculated gradient (mV/μm)	3.48	3.24	2.88	2.64
Measured gradient (mV/μm)	3.44	3.32	3.04	2.66
Error (%)	1.15	2.47	5.56	0.76

Fig. 8 shows the measured variation of the system output as a function of rod micromotion under the same input conditions as in Fig. 7, but with an extended range of axial displacement (-400 to 400 μm). Note that nonlinearity begins to emerge at offsets beyond about ±250 μm, due mostly to the onset of clipping in the amplifiers following the bridge. This suggests that implant micromotion can be detected and measured using this system in a range of at least -250 to 250 μm, which is adequate for most clinical applications. This value is in excess of the experimentally established lower limit of micromotion that, when exceeded, leads to the formation of connective tissue at the bone-implant interface. This is known to compromise the stability of fixation, and, ultimately, leads to implant loosening [28].

Table 1 provides a comparison between the measured and calculated gradients of the output voltage as a function of axial displacement, z . These results indicate that the system can estimate micromotion with an accuracy varying from 1% to over 6%, depending on initial gross displacement (migration). For an input voltage of amplitude 100 mV, the gradient of the post-calibration output voltage is in the range about 3–4 mV/μm. This is well above the noise floor of a typical CMOS amplifier emphasizing the practicality of the proposed system. The loss of accuracy in micromotion prediction with increasing implant migration (gross displacement) is discussed in the next section.

4.3. Large axial displacement (migration)

Tables 2 and 3 show measured and calculated values of R_1 , R_3 after calibration with respect to gross displacement of the rod (migration), at 100 and 12 kHz respectively. This data illustrates

Table 2

Comparison of calculated and measured values for R_1 , R_3 after calibration as a function of rod migration D at 100 kHz. All calculations and measurements are for $R_1 = R_2 = 400 \Omega$ and $R_3 = R_4 = 100 \Omega$ initially. The calculation results have 7 significant figures, while the measured results have 3 significant figures due to the limit of the testing equipment.

D (μm)	Calculated R_1, R_3 (Ω/Ω)	Measured R_1, R_3 (Ω/Ω)	R_1 error (%)	R_3 error (%)
0	405.5015/101.2881	402/101	0.86	0.28
100	412.223/103.1584	410/103	0.54	0.15
200	418.6361/104.9324	417/105	0.39	0.06
300	425.2956/106.7633	424/108	0.30	1.16
400	432.035/108.6151	430/110	0.47	1.28
500	438.9249/110.5321	437/112	0.44	1.33
600	445.9755/112.4824	445/115	0.22	2.24
700	453.0851/114.449	452/117	0.24	2.23
800	460.3083/116.4457	459/119	0.28	2.19
900	467.5202/118.4406	466/122	0.33	3.01
1000	474.9121/120.4837	472/124	0.61	2.92
1200	490.0047/124.6368	489/130	0.12	4.30
1400	505.5013/128.9315	505/135	0.10	4.71
1600	521.3331/133.2985	521/140	0.06	5.03
1800	537.4873/137.7543	537/146	0.08	5.99
2000	553.8521/142.2917	550/150	0.70	5.42
2250	574.8595/148.1057	575/159	0.02	7.36
2500	596.0424/153.9456	596/166	0.01	7.83
2750	617.7653/159.9758	619/174	0.20	8.77
3000	639.6718/166.0209	637/180	0.42	8.42
3500	683.8052/178.224	686/197	0.32	10.54
4000	727.6318/190.3681	731/213	0.46	11.89

Table 3

Comparison of calculated and measured values for R_1 , R_3 after calibration as a function of rod migration D at 12 kHz. All calculations and measurements are for $R_1 = R_2 = 40 \Omega$ and $R_3 = R_4 = 10 \Omega$ initially. The calculation results have 6 significant figures, while the measured results have 3 significant figures due to the limit of the testing equipment.

D (μm)	Calculated R_1 , R_3 (Ω/Ω)	Measured R_1 , R_3 (Ω/Ω)	R_1 error (%)	R_3 error (%)
0	40.6177/10.1125	40.6/10.1	0.04	0.12
100	41.1829/10.362	41.2/10.2	0.04	1.56
200	41.8409/10.6624	41.9/10.5	0.14	1.52
300	42.4614/10.9513	42.6/10.8	0.33	1.38
400	43.0956/11.2428	43.2/11.0	0.24	2.16
500	43.7361/11.5348	43.9/11.4	0.37	1.17
600	44.3957/11.8329	44.6/11.9	0.46	0.57
700	45.0549/12.136	45.3/12.0	0.54	1.12
800	45.7204/12.4326	46.1/12.3	0.83	1.07
900	46.3974/12.7443	46.8/13.1	0.87	2.79
1000	47.0856/13.0667	47.5/13.6	0.88	4.08
1200	48.489/13.7012	49.1/14.1	1.26	2.91
1400	49.9135/14.3599	50.5/14.8	1.18	3.06
1600	51.3739/15.0194	52.1/15.6	1.41	3.87
1800	52.8632/15.7059	53.7/16.4	1.58	4.42
2000	54.369/16.3884	55.3/17.3	1.71	5.56
2250	56.3036/17.2787	57.3/18.2	1.77	5.33
2500	58.253/18.1613	59.5/19.2	2.14	5.72
2750	60.2451/19.0798	61.6/20.2	2.25	5.87
3000	62.2318/19.9792	63.7/21.3	2.36	6.61
3500	66.2551/21.7486	68.0/23.3	2.63	7.13
4000	70.2351/23.6486	72.3/25.5	2.86	7.32

the 1-to-1 mapping between the values of R_1 , R_3 and rod migration (D), which has already been alluded to and which enables migration to be calculated with knowledge of either R_1 or R_3 . The derivation of an analytical expression relating these variables is detailed in Appendix B. In practice, it is more convenient to construct a look-up table based on Table 2 to estimate the value for D (this approach lends itself well to an automated version of the system). The range of migration prediction available is about 0 to ± 4 mm, with a limiting resolution of about $17 \mu\text{m}$, as indicated in Table 2. This value is calculated from the limiting resolution of the instrument used to measure R_1 (1Ω). Note that, as shown in Fig. 9, the errors between the measured and calculated values of R_1 , R_3 , in particularly for R_3 , increase rapidly with the rod migration (from 0.28% at $D=0$ to 11.89% at $D=4$ mm), contributing to the errors in migration and subsequent micromotion measurement. Furthermore, errors of R_1 at $f=12$ kHz are greater than those at $f=100$ kHz, while errors in R_3 are lower.

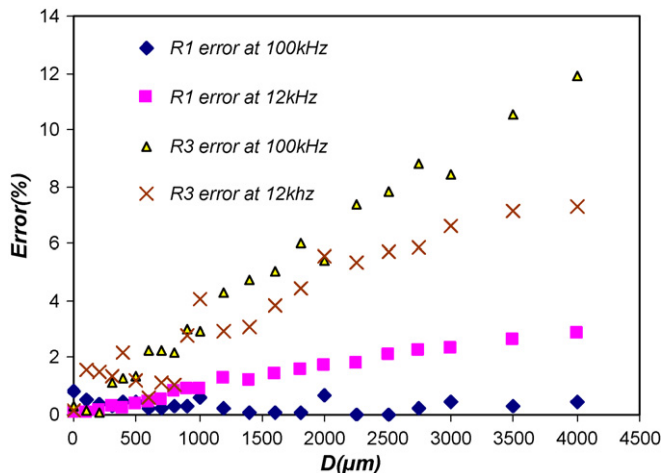


Fig. 9. Errors between calculated and measured values of R_1 , R_3 as a function of gross displacement (migration) D at 12 and 100 kHz, respectively (see also Tables 2 and 3).

5. Discussion

5.1. Overview of the device and its operation

In this paper we have described an RL bridge-based technique which enables small axial displacements ($\approx 1 \mu\text{m}$) of a rod to be measured about a pre-determined zero reference point. The zero reference point can have an axial displacement of about ± 4 mm with respect to the global reference, which is the geometrical centre of the device. The process is analogous to large- and small-signal analysis in conventional analogue circuit theory, since whilst the gross axial displacement requires a nonlinear description, the small displacements can be characterised using linear models.

The bridge consists of a pair of coaxial cylindrical coils into which a ferrite core is inserted, attached to a rod which links the bridge to the external system whose axial displacement is to be measured. We have shown that the coils can be miniaturised to the point where the complete system (which also includes signal processing and telemetry subsystems) is of a dimension suitable for use in clinical applications such as *total hip arthroplasty* (THA) and *total knee arthroplasty* (TKA), although other, non-clinical applications are possible.

A very important feature of the device is that measurement accuracy for small displacements is preserved across the prescribed range of gross axial displacement, relaxing the constraints on component tolerances and surgical assembly. This is possible due to a self-calibration algorithm which automatically adjusts certain parameters of the device (operating frequency, two variable resistors R_1 and R_3), automatically nulling the output of the bridge to a pre-determined limit (see Section 3) and setting the ‘operating point’ for the measurement of small displacements. The measured voltages are converted into axial displacements using the gradient of the output voltage at the operating point defined by the gross displacement D . The value of D can be found from the new values of the variable resistors R_1 and R_3 (i.e. R_1' and R_3') after the completion of the calibration process. Although the values of these resistors relate uniquely to the gross displacement D , the relationship between them is nonlinear and it is suggested that the use of a look-up table is an effective way of performing this calculation.

The significance of this process is that large and small displacements are accessible separately, leading naturally to the recording of *migration* and *micromotion* in orthopaedic prostheses, which is the principal application suggested here. The properties of the calibration algorithm are described in some detail in Section 5.2.

The calculation of both the large and small signal displacements requires analysis which relies on certain assumptions and approximations. A natural consequence of this is that the measurement accuracy is limited. The sources of potential error are listed in Section 5.3.

5.2. Properties of the calibration algorithm

In the calibration section it was noted that the calibration algorithm consists of *three* steps. For this process to be successful, it is necessary for the equations $REAL=0$ and $IMAG=0$ to have real solutions (see Eqs. (1), (A.9) and (A.10)). In addition, the algorithm must converge in the sense that the termination criterion is ultimately satisfied after N iterations, where N is finite. Table 4 shows the number of iterations N required for different values of the coupling coefficient k and the initial value of ΔL , the difference between L_1 and L_2 , where $L_1=L_0+\Delta L/2$, $L_2=L_0-\Delta L/2$, $L_0=800 \mu\text{H}$ and $R_{1,3}$ lie in the range 0–1 k Ω . All the data are collected from MATLAB-based simulations.

Note: the coils L_1 and L_2 can be connected in-phase or in anti-phase. We refer to these as Type I and Type II respectively. In Table 4,

Table 4

The number of iterations (N) required for successful bridge calibration as a function of k and ΔL . N/A means the algorithm does not converge and so calibration is impossible; all calculations are for $R_1 = R_2 = 400 \Omega$, $R_3 = R_4 = 100 \Omega$ and $f = 100$ kHz.

k	ΔL (μH)							
	0	20	100	200	300	400	500	600
-0.9	0	2	2	2	2	2	3	3
-0.8	0	2	2	2	2	2	3	3
-0.7	0	2	2	2	2	3	3	3
-0.5	0	2	2	3	3	3	3	4
-0.2	0	2	3	3	3	3	4	4
0	0	2	3	3	3	3	4	4
0.2	0	2	3	3	3	3	3	N/A
0.5	0	2	4	4	5	N/A	N/A	N/A
0.7	0	3	4	6	N/A*	N/A	N/A	N/A
0.8	0	3	5	N/A	N/A	N/A	N/A	N/A
0.9	0	3	N/A	N/A	N/A	N/A	N/A	N/A

* N/A means the calibration algorithm does not converge.

negative values of k represent a Type I connection and positive values of k represent Type II (see also Appendix A).

Table 4 illustrates that when k is positive, the number of iterations N increases monotonically with both k and ΔL . With k negative, N increases more slowly. Furthermore, for k positive and with certain values of ΔL , the calibration fails when k exceeds a threshold value. In this case, the maximum allowable values of k (k_{max}) for successful calibration are shown in Table 5. It can be seen that there is an inverse correlation between k_{max} and ΔL .

As a result of this observation, in our system the coils are connected so that $k < 0$ and the so bridge can always be calibrated. Using our present measuring system it is difficult to measure N with high precision. This is due to the fact all adjustments are carried out manually using multi-turn potentiometers. The collection of accurate values of N will be much facilitated by the use of an automatic calibration system, probably employing a microcontroller, which is under construction at the present time and which is discussed in outline below.

5.3. Summary of error sources

Gross displacement (migration) calculation:

Instrument errors: the LCR meter used to determine L_1 and L_2 is accurate to about 0.05%.

Flux leakage from L_1 and L_2 which is dependent on the position of the ferrite core, invalidating the model equations for the bridge.

Small displacement (micromotion) calculation:

Amplifier nonlinearity: for the largest values considered ($\pm 400 \mu\text{m}$) the amplifier output exceeded 1 V and the onset of clipping was becoming noticeable.

Flux leakage: (same comment as migration).

Errors affecting both measurements:

VCO output harmonic distortion: although the range of tuning of the VCO is relatively small (approximately 50–200 kHz) the resulting harmonic distortion will be larger than for than for an optimized

Table 5

The maximum values of coupling coefficient (k_{max}) that allows successful calibration of the bridge.

ΔL (μH)	20	100	200	300	400	500	600
k_{max}	0.975	0.855	0.713	0.572	0.430	0.285	0.132

fixed-frequency unit. However, simulations and measurements indicate that the presence of levels of 2nd and 3rd harmonic distortion as high as 1% had no noticeable effect on the calibration algorithm.

Component temperature variation: the system employs several types of components (resistors, inductors, etc.) with significant temperature coefficients. However, since body temperature is very stable ($\pm 1^\circ\text{C}$, in the absence of infection) this is unlikely to be a problem. In addition, any changes could be immediately corrected by running an extra calibration process.

It is also worth noting that since the small displacement measurements were made using an oscilloscope with a maximum resolution of ± 2 mV, with an amplifier gain of 500, the maximum axial resolution is about $\pm 0.5 \mu\text{m}$.

5.4. Automated implementation

The measurements described in this paper were made manually, i.e. the resistors R_1 and R_3 were implemented as multi-turn potentiometers which were adjusted by hand against the output which was monitored on an oscilloscope. The nature of the calibration algorithm described in Section 3 and the simple adjustments which are required to implement it lends itself well to an automated realization using a microcontroller. This could be integrated with the rest of the electronics or alternatively kept separate and mounted on a small board.

The main circuits/subsystems (in addition to the microcontroller) required in the design are (i) a voltage controlled oscillator (VCO), (ii) a phase detector, (iii) a phase *quadrature* detector and (iv) two fixed resistors (values 400 and 100 Ω) and two variable resistors variable within the approximate range 10 Ω to 1 k Ω . Measurements indicate that variations of the variable resistor values with a step of 0.1 Ω are sufficient to achieve residual transfer function amplitude of 2×10^{-5} after calibration. This resolution can be obtained using a 16-bit microcontroller, which is readily and cheaply available.

Test structures based on all the required subsystems have been fabricated, using 0.35 μm CMOS technology and are in the process of being tested. The outline block diagram of a possible automated version of the system is shown in Fig. 10.

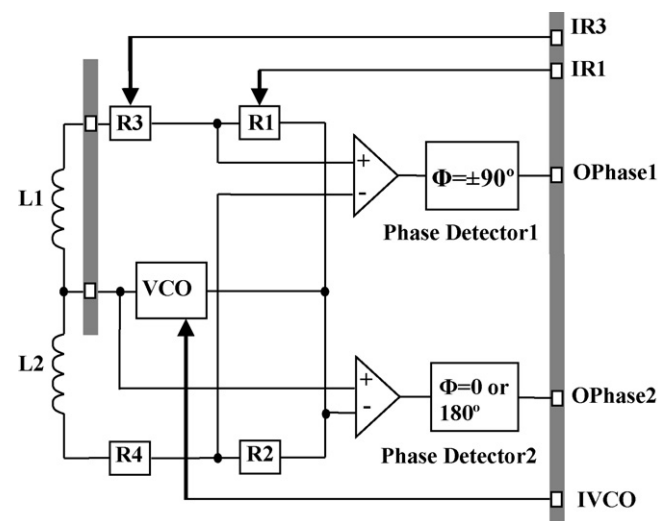


Fig. 10. Proposed hardware realization of the device. The component references correspond to Fig. 2 while the connections to the right of the figure are the inputs and outputs to a microcontroller.

5.5. Practical application

Patients will be assessed post-operatively during a clinic visit, in accordance with normal patient follow-up protocols. The automatic calibration algorithm implemented within the device allows *migration* and *micromotion* measurements to be made over an extended period of time. Follow-up assessment dates can be interspaced by a few days in the immediate post-operative period, to a few months in the medium term, usually within one year of the surgical procedure, and annually, biannually or at longer intervals thereafter [29]. At the beginning of each assessment visit, the system would be calibrated enabling the gross axial displacement (*migration*) since the last calibration to be recorded. Since body temperature is very stable ($\pm 1^\circ\text{C}$, in the absence of infection) the measured change recorded at the time of each calibration is a reliable measurement of gross axial shift (*migration*). During the follow-up visit to the clinic *micromotion* would be measured as the patient performs normal daily living activities such as, for example, walking and many samples could be collected during each gate cycle.

6. Conclusions and future work

This paper has described the principles of a method which allows the remote measurement of both large (order of mm) and small (order of μm) displacements of an implanted motion sensor. Although intended initially for the measurement of micromotion and migration in hip (THA) or knee (THK) prostheses, there are many other potential applications. Analysis is validated with preliminary measured results (from bench tests) and good agreement was reported.

At present an integrated version of the system is being developed for *in vitro* testing in the laboratory. A two-chip solution is being considered for this consisting of a full-custom design containing all the electronic components and subsystems except the microcontroller, realised in $0.35\ \mu\text{m}$ CMOS technology. The full-custom chip together with the microcontroller will be mounted on a small board. For future *in vivo* evaluations and eventual clinical application, a telemetry system will also be required, although this aspect is not considered in this paper.

Acknowledgement

The support of the Engineering and Physical Sciences Council (EPSRC) UK is gratefully acknowledged.

Appendix A. Transfer function of the bridge shown in Fig. 2

Appendices: These appendices contain approximate derivations of certain results used elsewhere in the text. The methods presented are based on an idealised (i.e. first-order) model of the coupled inductors L_1 and L_2 (mutual inductance M). Appendix A contains the derivation of the bridge transfer function discussed in Section 2; Appendix B analyses the convergence of the self-calibration algorithm (see Section 3) and Appendix C provides a method for estimating the initial values of the resistors.

As $M \neq 0$, the voltages appearing across L_1, L_2 are¹:

$$\begin{cases} V_{L_1} = j\omega L_1 I_1 - j\omega M I_2 \\ V_{L_2} = j\omega L_2 I_2 - j\omega M I_1 \end{cases} \quad (\text{A.1})$$

¹ The negative signs in eqn A1 relate to M and k positive, i.e. a Type II connection of the coils in which the effect of coupling is to reduce the voltages across L_1 and L_2 . In a Type I connection M and k are negative and the signs in the equation are inverted. In practice, as discussed in Section 4 of the paper, a Type I connection generally ensures more rapid and reliable convergence of the self-calibration process.

The input voltage of the bridge, V_{in} , is therefore:

$$V_{in} = (R_1 + R_3)I_1 + V_{L_1} = (R_2 + R_4)I_2 + V_{L_2} \quad (\text{A.2})$$

where the parasitic resistances of the coils, r_L , is absorbed into the values of R_3 and R_4 .

Substitute (A.1) into (A.2) and eliminate V_{L_1} and V_{L_2} :

$$I_2 = \frac{R_1 + R_3 + j\omega(L_1 + M)}{R_2 + R_4 + j\omega(L_2 + M)} I_1 = UI_1 = (a + jb)I_1 \quad (\text{A.3})$$

where

$$U(j\omega) = \frac{R_1 + R_3 + j\omega(L_1 + M)}{R_2 + R_4 + j\omega(L_2 + M)} = a + jb \quad (\text{A.4})$$

Hence Eq. (A.2) can be written as

$$V_{in} = [R_1 + R_3 + j\omega(L_1 - UM)]I_1 \quad (\text{A.5})$$

Using Eqs. (A.3) and (A.5), the output voltage of the bridge can be calculated:

$$V_{o\text{-bridge}} = R_1 I_1 - R_2 I_2 = V_{in} \frac{R_1 - UR_2}{R_1 + R_3 + j\omega(L_1 - UM)} \quad (\text{A.6})$$

Substitute (A.4) into (A.6), the transfer function of the bridge is:

$$H_1(j\omega) = REAL + j.IMAG \quad (\text{A.7})$$

and the output voltage of the bridge (including the amplifier), V_o is:

$$V_o = A_v \cdot H_1(j\omega) \cdot V_{in} = A_v \cdot (REAL + j.IMAG) \cdot V_{in} \quad (\text{A.8})$$

where A_v is amplifier gain (assumed to be frequency independent) and

$$REAL = \frac{(R_1 - aR_2)(R_1 + R_3 + \omega bM) - bR_2\omega(L_1 - aM)}{(R_1 + R_3 + \omega bM)^2 + \omega^2(L_1 - aM)^2} \quad (\text{A.9})$$

$$IMAG = \frac{-bR_2(R_1 + R_3 + \omega bM) - \omega(R_1 - aR_2)(L_1 - aM)}{(R_1 + R_3 + \omega bM)^2 + \omega^2(L_1 - aM)^2} \quad (\text{A.10})$$

where

$$a = \frac{(R_1 + R_3)(R_2 + R_4) + \omega^2(L_1 + M)(L_2 + M)}{(R_2 + R_4)^2 + \omega^2(L_2 + M)^2} \quad (\text{A.11})$$

$$b = \frac{\omega[(R_2 + R_4)(L_1 + M) - (R_1 + R_3)(L_2 + M)]}{(R_2 + R_4)^2 + \omega^2(L_2 + M)^2} \quad (\text{A.12})$$

Appendix B. Convergence analysis for the calibration process shown in Section 3.1

As noted in the calibration section, the second step is to adjust the potentiometers R_1 and R_3 alternatively in each iteration to make *REAL* or *IMAG* zero until $|H_1(j\omega)|$ approaches zero. Let $R_{1,n}$ and $R_{3,n}$ represent the calibrated values of R_1 and R_3 at n th iteration, which means $R_{1,n}$ and $R_{3,n-1}$ produces result of zero for *REAL*, while $R_{1,n}$ and $R_{3,n}$ produces result of zero for *IMAG*.

That is,

$$\begin{cases} REAL(R_{1,n}, R_{3,n-1}) = 0 \\ IMAG(R_{1,n}, R_{3,n}) = 0 \end{cases} \quad (\text{B.1})$$

Substituting (A.9) into (B.1), the relationships between $R_{1,n}$ and $R_{3,n}$ then can be written as

$$\begin{cases} R_{1,n} = \frac{1}{2A_1} \left[A_3 - A_2 R_{3,n-1} + (A_7 R_{3,n-1}^2 + A_8 R_{3,n-1} + A_9)^{1/2} \right] \\ R_{3,n} = \frac{1}{2B_1} \left[B_3 - B_2 R_{1,n} + (B_7 R_{1,n}^2 + B_8 R_{1,n} + B_9)^{1/2} \right] \end{cases} \quad (\text{B.2})$$

where $A_{1-3,7-9}$ and $B_{1-3,7-9}$ are functions of $R_{2,4}, L_{1,2}, M$ and ω .

The two equations in (B.2) can be simplified by expanding $(A_7 R_{3,n-1}^2 + A_8 R_{3,n-1} + A_9)^{1/2}$ and $(B_7 R_{1,n}^2 + B_8 R_{1,n} + B_9)^{1/2}$ using a

Taylor series expansion about the real numbers E_1 and E_2 , if E_1 and E_2 are sufficiently close to $R_{3,n-1}$ and $R_{1,n}$:

$$(A_7 R_{3,n-1}^2 + A_8 R_{3,n-1} + A_9)^{1/2} = (A_7 E_1^2 + A_8 E_1 + A_9)^{1/2} + \frac{1}{2}(A_7 E_1^2 + A_8 E_1 + A_9)^{-1/2} (2A_7 E_1 + A_8)(R_{3,n-1} - E_1) + Rm_1$$

and

$$(B_7 R_{1,n}^2 + B_8 R_{1,n} + B_9)^{1/2} = (B_7 E_2^2 + B_8 E_2 + B_9)^{1/2} + \frac{1}{2}(B_7 E_2^2 + B_8 E_2 + B_9)^{-1/2} (2B_7 E_2 + B_8)(R_{1,n} - E_2) + Rm_2$$

where Rm_1 and Rm_2 are remainder terms.

To simply (B.3), the following two assumptions are made based on analysis above:

- (i) $E_1 = (d/d_{max}) * [(R_{3,\infty})_{dmax} - (R_{3,\infty})_{dmin}] + (R_{3,\infty})_{dmin}$,
 $E_2 = (d/d_{max}) * [(R_{1,\infty})_{dmax} - (R_{1,\infty})_{dmin}] + (R_{1,\infty})_{dmin}$ with
 $0 < n < \infty$, where d is the initial gross displacement (migration),
 d_{min} and d_{max} are minimum and maximum allowable migration
 (in our test it is 0 and 4 mm respectively), $(R_{1,\infty})_{dmin}$ and
 $(R_{3,\infty})_{dmin}$ are values for $R_{1,3}$ when n approaches infinity at
 $D = d_{min}$, and $(R_{1,\infty})_{dmax}$ and $(R_{3,\infty})_{dmax}$ are values for $R_{1,3}$ when
 n approaches infinity at $D = d_{max}$.
- (ii) Rm_1 and Rm_2 can both be ignored.

Based on these two assumptions, (B.2) can be reduced as follows by substituting (B.3) to (B.2):

$$R_{1,n} \approx X_0 + X_1 R_{3,n-1} \quad n \geq 1$$

$$R_{3,n} \approx Y_0 + Y_1 R_{1,n} \quad n \geq 1$$

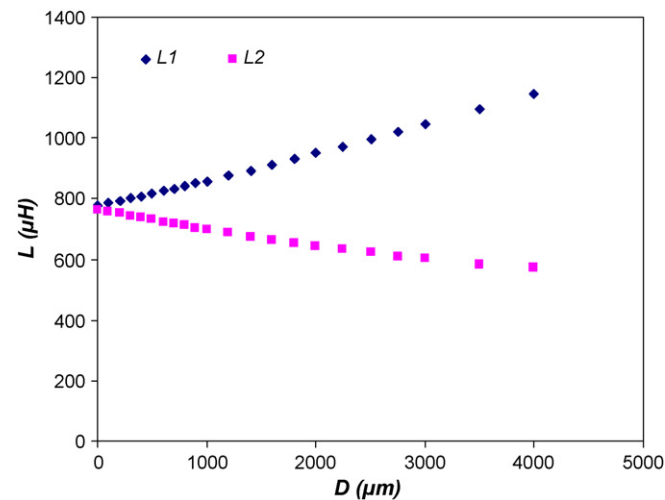


Fig. B1. Inductance of L_1, L_2 as a function of migration D between 0 and 4 mm.

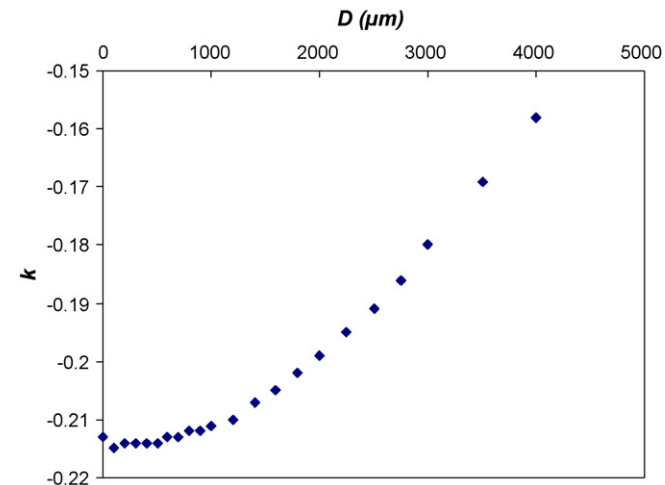


Fig. B2. Coupling coefficient k as a function of migration D between 0 and 4 mm.

where $X_{0,1}$ and $Y_{0,1}$ are functions of $A_{1-3,7-9}$, $B_{1-3,7-9}$ and $E_{1,2}$.

Substitute the expression of $R_{3,n}$ into the expression of $R_{1,n}$ in (B.4), therefore the expression of $R_{1,n}$ as a function of $R_{1,0}$ is:

$$R_{1,n} \approx \begin{cases} X_0 + X_1 R_{3,0}; & n = 1 \\ \sum_{m=0}^{n-2} (X_1 Y_1)^m (X_0 + X_1 Y_0) + (X_1 Y_1)^{n-1} R_{1,1}; & n > 1 \end{cases}$$

$$R_{3,n} \approx \sum_{m=0}^{n-1} (X_1 Y_1)^m (Y_0 + X_0 Y_1) + (X_1 Y_1)^n R_{3,0}; \quad n \geq 1$$

It is apparent that $R_{1,n}$ and $R_{3,n}$ converge towards a limiting value as n approaches infinity if $|X_1 Y_1| < 1$. This limit corresponds to zeros of the functions *REAL* and *IMAG* (B.1) and hence the null-point of the bridge. To show convergence, it is sufficient (but not necessary) to show that $|X_1 Y_1| < 1$.

The plots of individual inductance of L_1, L_2 and coupling coefficient k as a function of migration (D) are shown in Figs. B1 and B2. The expression of $|X_1 Y_1|$, however, is a high-order function of L_1, L_2 and k , which varies with the initial displacement of the rod (migration). Here we examine the inequality $|X_1 Y_1| < 1$ using a graphical method. The plot of $|X_1 Y_1|$ as a function of the initial migration (Fig. B3) shows that the value of $|X_1 Y_1|$ is less than 1 with the initial migration between 0 to 4 mm. In conclusion, the bridge can be calibrated after a finite number of iterations with the initial migration from 0 to 4 mm.

As shown in (B.5), when $n \rightarrow +\infty$, the values of $R_{1,n}$ and $R_{3,n}$ are:

$$R_{1,\infty} \approx \frac{X_0 + X_1 Y_0}{1 - X_1 Y_1}$$

$$R_{3,\infty} \approx \frac{Y_0 + X_0 Y_1}{1 - X_1 Y_1}$$

The accuracy validation of Eq. (B.6) is illustrated in Fig. B4 by comparing the calibrated values for R_1, R_3 calculated from Eq. (B.6) and those from Eq. (B.1). The low errors (<0.08%) between two groups of

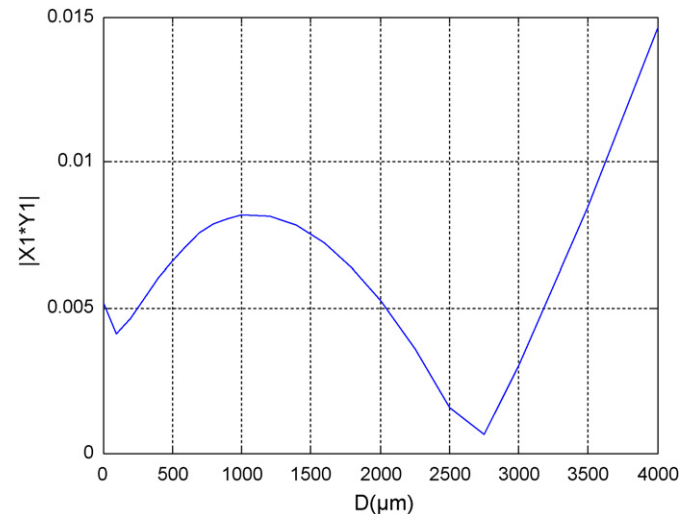


Fig. B3. $X_1 Y_1$ as a function of the initial migration (D) in the range 0–4 mm. It can be seen that $|X_1 Y_1| < 1$ throughout the range. Initially $R_1 = R_2 = 400 \Omega$, $R_3 = R_4 = 100 \Omega$ and $f = 100 \text{ kHz}$.

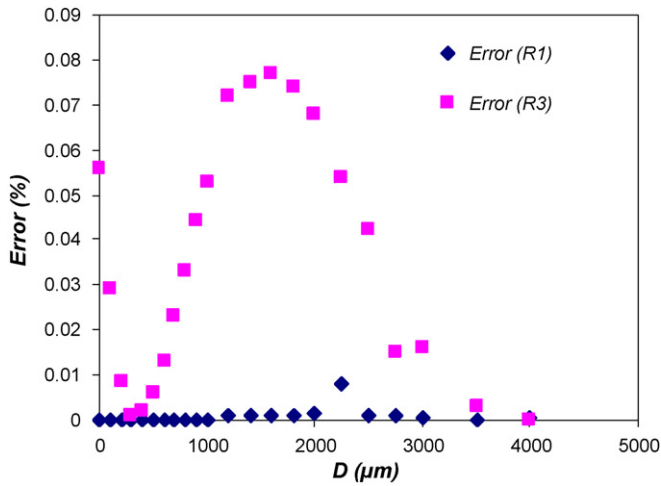


Fig. B4. Errors between the calibrated values for R_1 , R_3 calculated from Eq. (B.6) and those from Eq. (B.1) as a function of migration D . Initially $R_1 = R_2 = 400 \Omega$, $R_3 = R_4 = 100 \Omega$ and $f = 100$ kHz.

values validate not only Eq. (B.5) and (B.6) as formulas for values of R_1 , R_3 after calibration, but also the two assumptions made above for the simplification of (B.2).

Appendix C. Choice of the resistor values R_2 and R_4

As noted in Section 3, the operation of the calibration algorithm is much simplified if two of the resistors in the RL bridge are fixed, say R_2 and R_4 . To determine suitable values for these components, consider the first step in the calibration algorithm which chooses the resonant frequency of the bridge by setting the function $IMAG = 0$. In the simplest case when $M = 0$ and assuming that $R_1 = R_2$ and $R_3 = R_4$, the expression for resonance reduces to:

$$(R_2 + R_4)^2 - \omega^2 L_1 L_2 = 0 \tag{C.1}$$

For $f = 100$ kHz and $L_1 = L_2 = 800 \mu H$, $(R_2 + R_4) \approx 500 \Omega$. MATLAB simulations indicate that even for $M \neq 0$, these typical values change very little. Also, due to the effects of the calibration, the values are not critical.

Table C1 examines the convergence of the system as a function of the ratio R_1/R_3 ($=ra$) and gross displacement, D . This indicates that for a particular value of D there is a shallow minimum in the number of iterations required when $ra \approx 4$. Since $R_2 + R_4 = 500 \Omega$, we choose $R_2 = 400 \Omega$ and $R_4 = 100 \Omega$.

Table C1

Relationship between the number of iterations required by the calibration process for convergence and the initial choice of resistors ($R_1 = R_2$ and $R_3 = R_4$; $R_1 + R_3 = 500 \Omega$, $f = 100$ kHz). The parameter $ra = R_1/R_3$. The dependence on gross displacement D is also shown.

ra	D (mm)				
	0	1	2	3	4
0.1	1	2	3	3	4
1	1	3	3	3	3
2	1	2	3	3	3
3	1	2	2	3	2
4	1	2	2	2	3
5	1	2	2	2	3
6	1	2	2	3	3
7	1	2	2	3	3
8	1	2	2	3	3
9	1	2	2	3	3
10	1	2	2	3	3

References

- [1] "History of Total Hip Replacement," <http://www.thehipdoc.com/history.htm>.
- [2] No authors listed, 2002/034 NICE recommends the selective use of metal on metal hip resurfacing, <http://www.nice.org.uk/page.aspx?o=33569> (date last accessed 23.07.07).
- [3] "Knee Replacement," <http://www.nhs.uk>.
- [4] G. Hawker, et al., Health-related quality of life after knee replacement, J. Bone Joint Surg. Am. 80-A (1998) 163–173.
- [5] O. Robertsson, M. Dunbar, T. Pehrsson, K. Knutson, L. Lidgren, Patient satisfaction after knee arthroplasty: a report on 27,372 knees operated on between 1981 and 1995 in Sweden, Acta Orthop. Scand. 71 (2000) 262–267.
- [6] C.Y. Ng, J.A. Ballantyne, I.J. Brenkel, Quality of life and functional outcome after primary total hip replacement: a five-year follow-up, J. Bone Joint Surg. Br. 89-B (2007) 868–873.
- [7] R.D. Ramiah, A.M. Ashmore, E. Whitley, G.C. Bannister, Ten-year life expectancy after primary total hip replacement, J. Bone Joint Surg. Br. 89-B (2007) 1299–1302.
- [8] G. Garellick, H. Malchau, P. Herberts, E. Hansson, H. Axelsson, T. Hansson, Life expectancy and cost utility after total hip replacement, Clin. Orthop. 346 (1998) 141–151.
- [9] R. Chang, J.M. Pelligier, G.B. Hazen, A cost-effectiveness analysis of total hip arthroplasty for osteoarthritis of the hip, JAMA 275 (1996) 858–865.
- [10] C.S. Ranawat, J. Insall, J. Shine, Duo-condylar knee arthroplasty. Hospital for special surgery design, Clin. Orthop. 120 (1976) 76–82.
- [11] M.D. Skolnick, M.B. Coventry, D.M. Ilstrup, Geometric total knee arthroplasty. A two-year follow-up study, J. Bone Joint Surg. 58-A (1976) 749–753.
- [12] E. Losina, J. Barrett, N.N. Mahomed, J.A. Baron, J.N. Katz, Early failures of total hip replacement: effect of surgeon volume, Arthritis Rheumat. 50 (2008) 1338–1343.
- [13] M. Nixon, G. Talor, P. Sheldon, S.J. Iqbal, W. Harper, Does bone quality predict loosening of cemented total hip replacements? J. Bone Joint Surg Br. 89-B (2007) 1303–1308.
- [14] D.M. Dall, I.D. Learmonth, M. Solomon, A scoring system to determine radiological loosening in cemented total hip arthroplasty, Int. Orthopaed. (SICOT) 16 (1992) 339–343.
- [15] J.R. Moreland, Mechanism of failure in total knee arthroplasty, Clin. Orthop. Relat. Res. 226 (1988) 49–64.
- [16] P. Ducheyne, A. Kagan, J.A. Lacey, Failure of total knee arthroplasty due to loosening and deformation of the tibial component, J. Bone Joint Surg. Am. 60 (1978) 384–391.
- [17] K. Hidakawa, J.J. Jacobs, R. Urban, T. Saito, Mechanisms of failure of total hip replacements: lessons learned from retrieval studies, Clin. Orthop. Relat. Res. 420 (2004) 10–17.
- [18] W. Görtz, U.V. Nagerl, H. Nagerl, M. Thomsen, Spatial micromovements of uncemented femoral components after torsional loads, J. Biomech. Eng. 124 (December (6)) (2002) 706–713.
- [19] J.R. Britton, C.G. Lyons, P.J. Prendergast, Measurement of the relative motion between an implant and bone under cyclic loading, Strain 40 (November (4)) (2004) 193–202.
- [20] J. Karrholm, H. Malchau, F. Snorrason, P. Herberts, Micromotion of femoral stems in total hip arthroplasty. A randomized study of cemented, hydroxyapatite-coated, and porous-coated stems with roentgen stereophotogrammetric analysis, J. Bone Joint Surg. Am. 76 (1994) 1692–1705.
- [21] D.W. Burke, D.O. O'Connor, E.B. Zalenski, M. Jasty, W.H. Harris, Micromotion of cemented and uncemented femoral components, J. Bone Joint Surg. Br. 73 (1991) 33–37.
- [22] S. Gheduzzi, A.W. Miles, A review of pre-clinical testing of femoral stem subsidence and comparison with clinical data, Proc. IMechE Part H: J. Eng. Med. 221 (1) (2007) 39–46.
- [23] P.A. Lotke, M.L. Ecker, Influence of positioning of prosthesis in total knee replacement, J. Bone Joint Surg. Am. 59 (1977) 77–79.
- [24] D.W. Bühler, T.R. Oxland, L.-P. Nolte, Design and evaluation of a device for measuring three-dimensional micromotions of press-fit femoral stem prostheses, Med. Eng. Phys. 19 (1997) 187–199.
- [25] S.A. Maher, P.J. Prendergast, Discriminating the loosening behaviour of cemented hip prostheses using measurements of migration and inducible displacement, J. Biomech. 35 (2002) 257–265.
- [26] S. Arana, E. Castaño, F.J. Gracia, High sensitivity linear position sensor developed using granular Ag–Co giant magnetoresistances, Sens. Actuators A 123 (2005) 116–121.
- [27] S. Hao, J.T. Taylor, A.W. Miles, C.R. Bowen, An implantable system for the in vivo measurement of hip and knee migration and micromotion, in: Proceeding of the ICSES '08 International Conference on Signals and Electronic Systems, 2008, pp. 445–448.
- [28] H. Kienapfel, C. Sprey, A. Wilke, P. Griss, Implant fixation by bony ingrowth, J. Arthroplasty 14 (1999) 355–368.
- [29] S.M. Teeny, S.C. York, J.W. Mesko, R.E. Rea, Long-term follow-up care recommendations after total hip and knee arthroplasty: results of the American association of hip and knee surgeons' member survey, J. Arthroplasty 18 (2003) 954–962.

Biographies

Shiyang Hao received the BSc degree from Peking University, China in 2004 and the MSc degree from University of Bath, UK in 2005. She is now doing PhD in Electronics and Electrical Engineering Department at University of Bath since 2005. The topic of her PhD is to design and optimization of telemetry and sensor integration for an implantable system. She has authored two conference papers.

John Taylor was born at Wanstead, Essex, UK, in 1952. He received the BSc and PhD degrees from Imperial College, London University, London, UK, in 1973 and 1984, respectively. He joined the Department of Electronic and Electrical Engineering at University College London in 1985 and subsequently, in 2002, the Department of Electronic and Electrical Engineering at the University of Bath, Bath, UK, where he holds the position of Professor of Microelectronics and Optoelectronics and Director of the University *Centre for Advanced Sensor Technologies*. His research interests are in the fields of analogue and mixed analogue and digital system design, including communication systems and low-power implantable systems for biomedical and rehabilitation applications. Professor Taylor has published more than 140 technical papers in international journals and conferences and has co-edited a handbook on filter design.

Chris Bowen is a Reader in materials at the Department of Mechanical Engineering, University of Bath. He obtained a DPhil from the University of Oxford on the pro-

cessing of ceramic composites. He undertook postdoctoral research at the Technical University of Hamburg-Harburg on ceramic composites and was a senior scientist at Defence Evaluation and Research Agency. His current research areas include electromechanical properties of functional materials and composites, materials for sensors and dielectric materials. He has over 80 papers in refereed journals.

Sabina Gheduzzi is a Lecturer the Department of Mechanical Engineering at the University of Bath where she obtained her PhD in 2001. Her current research can be summarised under the broad topic of implant fixation and interfaces in orthopaedics and represents the natural extension of the work initiated during her postgraduate training at the University of Bath. She has published over 20 refereed journal papers and over 50 refereed conference papers.

Anthony Miles is Professor of Biomechanics and Director of the Centre for Orthopaedic Biomechanics at the University of Bath. The Centre has a specific focus on pre-clinical assessment and validation of medical devices and surgical procedures spanning joint replacement, fracture fixation, bone augmentation and biomaterials. Professor Miles has extensive experience in biomechanics in relation to both total joint replacement and fracture, specifically relating to issues of implant fixation, loading and simulation. He has been actively involved in the development of surgical devices, instrumentation and surgical techniques that have been used or applied in clinical practice.